Supporting Information for "Variability in Records of Phanerozoic Seawater Sulfate," by T. M. Present, J. F. Adkins, and W. W. Fischer (2020).

Age assignment and data compilation

6710 $\delta^{34}S$ data of sulfate from Phanerozoic marine evaporites, bulk rock CAS, biogenic CAS, or marine barite were compiled from 108 references. Some previous evaporite $\delta^{34}S$ compilations included data from salt diapirs, secondary veins in non-sedimentary rocks, aqueous brines that had dissolved nearby evaporite-bearing formations, or brackish or non-marine depositional environments; these data were excluded from this compilation. The bulk rock CAS record contains data from sedimentary carbonate phases, although the extraction procedure employed varies between studies. The biogenic CAS record includes CAS data from brachiopods, belemnites, bivalves, and foraminifera, as well as sulfate in apatite from conodonts. Although preservation of biogenic and bulk-rock CAS was addressed in each reference, all data were included in the current compilation. Sulfur isotope data from authigenic phosphorites were not included.

For data from studies that included radiometric ages, the radiometric age model was maintained. For studies that included stage-level assignments of the lithostratigraphy, ages were assigned by linearly interpolating on stratigraphic thickness unless the reference included independent estimates of sedimentation rate. For studies that assigned ages but did not include stratigraphic data, ages were updated by linearly interpolating between the assigned ages of stage boundaries in each time scale. The $\delta^{34}S$ data and stratigraphic height or age assignment was extracted graphically from figures in references that did not tabulate data. Many evaporite deposits have substantially improved stratigraphic and age assignments since publication of their sulfur isotope data. The ages of evaporite-bearing formations have been updated using the most recent tectono-stratigraphy and/or economic exploration literature.

Histograms of the four compiled proxy datasets are shown in Supporting Figure S1, and summary statistics are reported in Supporting Table S1. Supporting Table S2 includes each data source and a description of the age model applied to the reference, with applicable citations. Supporting File *d34S_Data.xlsx* tabulates the compiled $\delta^{34}S$ data with the proxy material, assigned age, and data source.

Variography

Semivariance is the variance—per point—of the difference between equally spaced pairs of measurements (Webster & Oliver, 2007, p. 54). Variograms are functions relating semivariance to the distance between the points, called the lag. In this paper, the lag is the age difference between two samples. The empirical variogram describing the semivariance of the $\delta^{34}S$ data, γ, as a function of lag, h, is estimated for $N(h)$ pairs of data with that lag:

$$\gamma(h) = \frac{1}{2}\frac{1}{N(h)}\sum_{i=1}^{N(h)}[\delta^{34}S(t_i) - \delta^{34}S(t_i + h)]^2$$

Although the variance of pairs of data may change as a function of t, the semivariance does not. If the variance was not a function of t, then the semivariance would simply mirror the covariance (Webster & Oliver, 2007, p. 55).

Formulating variance as the square of the difference is sensitive to outliers in the data. By decreasing the order of the variogram estimator from 2 and applying a correction to maintain a normal distribution, a variogram that unweights tails on the distribution and thus is more robust to outliers is developed (Cressie & Hawkins, 1980). A variogram order of 0.5 was used here:

$$\gamma_{robust}(h) = \frac{1}{2}\frac{\left[\frac{1}{N(h)}\sum_{i=1}^{N(h)}\sqrt{|\delta^{34}S(t_i) - \delta^{34}S(t_i+h)|}\right]^4}{0.457 + \frac{0.494}{N(h)} + \frac{0.045}{N^2(h)}}$$

Empirical variograms for detrended $\delta^{34}S$ data from each proxy in each era are shown in Supporting Figure S2. Because timeseries are temporally autocorrelated, the semivariance at short lags is less than at long lags. Variograms of geologic eras have enough paired data to resolve the autocorrelation structure. The maximum variability over the domain of interest is described by the population variance, and the semivariance approaches this value over an interval called the range. The population variance is often referred to as the "sill" in geospatial analysis.

At the shortest lags, the semivariance is not zero. This uncorrelated variance represents the variability of $\delta^{34}S$ measurements unresolved by sampling. It is often referred to as the "nugget" in geospatial analysis.

The approach of semivariance to the population variance can be described with a model of the structure of the empirical variogram. For our 2-dimensional (time and $\delta^{34}S$) data, semivariance can be modelled by the overlap of two circles populated randomly following a Poisson distribution (Webster & Oliver, 2007, p. 87). This circular variogram model describes semivariance as a function of lag, h, given the range, a, sill, c, and nugget, n:

$$\gamma_{model}(h) = \begin{cases} n + c\left\{1 - \frac{2}{\pi}\cos^{-1}\left(\frac{h}{a}\right) + \frac{2h}{\pi a}\sqrt{1 - \frac{h^2}{a^2}}\right\} & \text{for } h \le a, \\ n + c & \text{for } h > a \end{cases}$$

To fit the variogram model to the empirical variogram, we diagnosed the nugget and sill from the data and visually adjusted the range: the nugget is the empirical semivariance computed at the mean minimum time between all pairs of data, and the sill is the population variance. We only require the model to estimate uncertainty in the $\delta^{34}S$ records—we are not attempting to predict $\delta^{34}S$ compositions in rocks that haven't been sampled. Therefore, it was unnecessary to employ more agnostic strategies to select a variogram model and fit it to the empirical variogram.

Other bounded variogram models, such as spherical and exponential models, produce nearly indistinguishable results. This is because model-independent descriptions of the data—the population variance and the empirical semivariance calculated at the mean minimum lag between data—bound the minimum and maximum kriging variance. The variogram model shape and range describe the weights of data between these bounds.

Kriging

Kriging is both a method of interpolating the data and for modelling the uncertainty around the unobserved, interpolated point (Gebbers, 2010). The expected value of an interpolated point is simply a weighted average of the data. The weights are calculated using the variogram model that describes semivariance as a function of distance from observations such that the estimated semivariance of the unobserved point (called the kriging variance) is minimized.

Detrending the data is necessary to ensure that the mean is constant (first-order stationary), but results in improper estimation of total variance by failing to account for both uncertainty and bias in the detrending (Lark & Webster, 2006). Therefore, kriging variance at long lags may be underestimated (by failing to include the uncertainty of the detrending model) or even overestimated (by biased sampling affecting the detrending model and failing to capture the minimum temporal variance in that region).

We model the variogram sill as the population variance, but clear mismatches in long-lag empirical variograms are apparent (Supplemental Figure S2), with some lag intervals having both much higher and much lower variance. In addition to a violation of first-order stationarity, we interpret this as a lack of knowledge of the structure of long-term $\delta^{34}S$ trends where it is not constrained by data, rather than a quantitative statement about its variance over long timescales. In other words, dramatic sulfur isotope excursions may be possible in unsampled intervals of geologic time, and there is no predictive power from the variance deriving from the amplitude of currently observed excursions. Our goal of using the kriged variance to describe the quality of $\delta^{34}S$ records is therefore critically different than using the kriged variance to predict $\delta^{34}S$ through time, in the way that kriging is often applied to predict spatial-temporal patterns in environmental and earth sciences.

On the other hand, the estimates of uncorrelated variance—that on short timescales—are generally well constrained by the data. For estimating kriging variance through time, the variogram model at short lags is much more important than at long lags. Over the observed range of correlation until semivariance matches or exceed population variance, most records in each time interval indeed show increasing semivariance with lag distance (Supporting Figure S2). Only one set of data, the Cenozoic bulk rock CAS record, has a negligible difference between uncorrelated and population variance. Constraints on either are therefore poor, but resultant kriging variance is insensitive to the exact shape of the variogram model.

Timeseries variography and kriging of synthetic data

Variography and kriging can usefully describe the structure of variance of timeseries $\delta^{34}S$ data. In addition to differences between the proxy records inherent to each geologic archive, some variance in the records may derive from misalignment of age models.

The dashed line in Supporting Figure S3a represents a synthetic isotope excursion similar in duration and magnitude to some reported in the Paleozoic, such as during the Cambrian SPICE interval (e.g., Gill et al., 2007). The orange dots represent samples taken randomly in time from a population that follows the synthetic excursion with synthetic Gaussian noise with a standard deviation of 2‰. The variogram captures a 1‰ 1σ standard deviation of uncorrelated variance at the shortest lag interval and approaches the population variance (*ca.* 5‰) of the synthetic data over

a range of approximately 500 kyr. Applying a circular variogram model and kriging the random samples results in the gray kriged estimate.

But, given multiple aligned records, how much of the variogram structure is attributable to the inherent "noise" in the archive (illustrated in Supporting Figure S3a) and how much is attributable to poor temporal alignment? Supporting Figures S3b and S3c test this by overlaying the synthetic record in Supporting Figure S3a with randomly misaligned records. Supporting Figures S3b represents poor alignment of multiple identical records sampled at different localities by randomly misaligning the full excursion within the average length of a Paleozoic stage (5.5 Myr). Although the kriged estimate of the interpolated record and the variogram are clearly different than the true synthetic excursion, the uncorrelated variance and population variance are only slightly larger. These are robust statistical descriptions of the uncertainty in the data.

Similarly, an unconformity or uneven sedimentation rate may change the amplitude or shape of an isotope excursion if, when sampling, this is unknown. Supporting Figure S3c shows how randomly varying the amplitude of the excursion in Supporting Figure S3a with a standard deviation of 25% also does not dramatically increase the nugget or sill variance.

Uncorrelated variance's sensitivity to age misalignment is further shown in Supporting Figure S4. Different combinations of 1 to 5 synthetic records randomly misaligned with standard deviations of 1 to 10 Myr were each simulated 25 times, and the average nugget effect was calculated. This bootstrapping approach estimates the expected nugget effect solely related to poor age models. More misaligned records result in a larger nugget in the composite record, and the magnitude of the nugget is maximized if the isotope excursions are, on average, exactly out of phase (i.e., misaligned by half of the duration of the $\delta^{34}S$ excursion, modelled as 2 Myr in Supporting Figure S4).

In summary, it is likely that the increase in both uncorrelated (nugget) and population (sill) variance of all records with age represents both poorer age control in older strata, and also a meaningful change in the variability of ancient rocks due to changes in how sulfate is incorporated and preserved.

Supporting Figures, Tables, and Files

Supporting Figure S1. *Histograms of all compiled $\delta^{34}S$ data of sulfate in each proxy for ancient seawater sulfate with means and 1σ standard deviations. Arrows mark bins with 1 to 10 counts, and the broken line marks the means.*

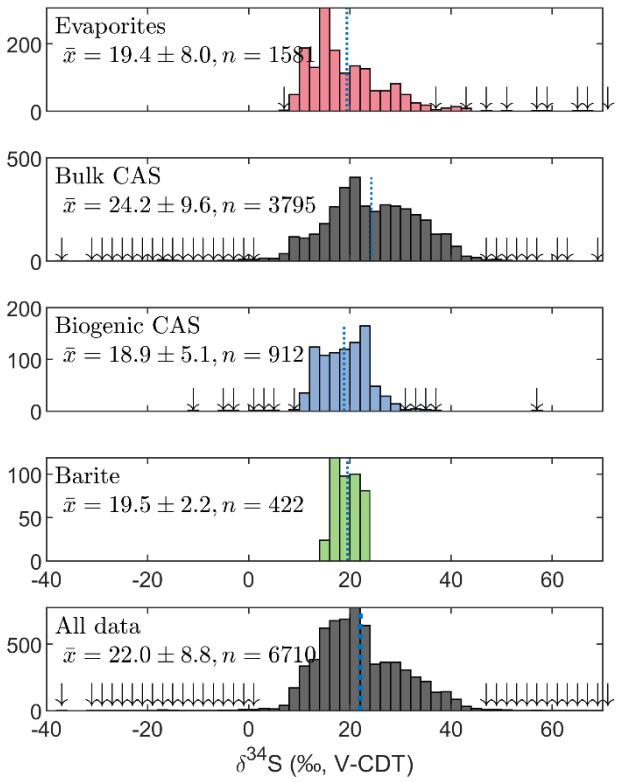

Supporting Figure S2. *Empirical variograms showing semivariance as a function of lag times less than 40 Myr for each record, and for each record by geologic age. The dashed horizontal line is the population variance of all data within the 1st and 99th percentile of the linearly detrended $\delta^{34}S$ data, which is used to estimate the sill for the circular variogram model (green solid line). The unresolved variance for each record is the semivariance at the shortest lag, computed at the mean minimum time between all pairs of data within the 1st and 99th percentile of the linearly detrended $\delta^{34}S$ data.*

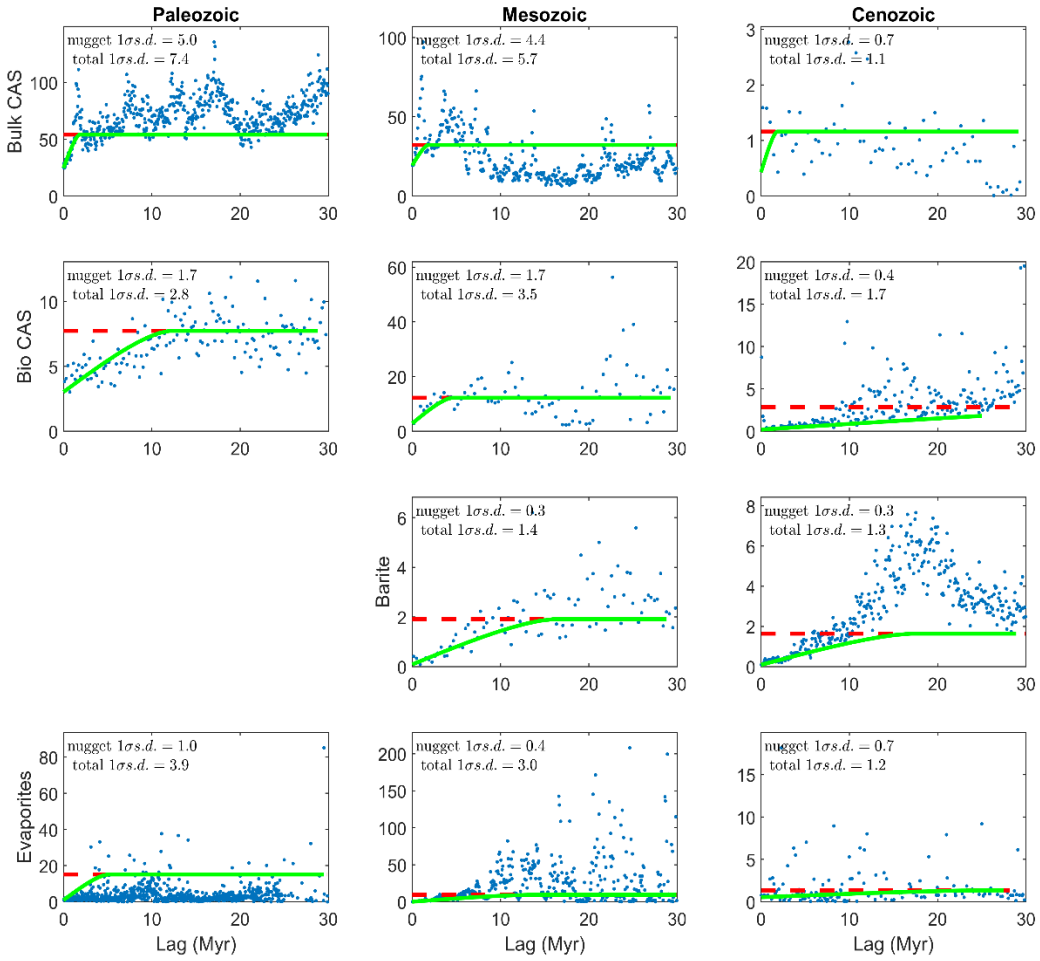

Supporting Figure S3. *Synthetic data to examine the effect sampling and age modelling on the variogram of a global isotope excursion sampled at multiple localities. All sampling and age model artifacts lead to less than 3‰ nugget effects, which may account for a source of unresolved variance in many proxy records but cannot explain all unresolved variance in the Phanerozoic.* ***(a)*** *Imprecise sampling represented by Gaussian noise with a standard deviation of 2‰ added to a synthetic $\delta^{34}S$ excursion with 20‰ amplitude over 2 Myr, like some Paleozoic excursions in CAS data.* ***(b)*** *Imprecise age alignment represented by precise sampling of multiple randomly aligned but otherwise identical excursions varying within the average length of a Paleozoic stratigraphic stage (standard deviation of 5.5 Myr).* ***(c)*** *Inaccurate age model represented by randomly varying amplitude with 5‰ standard deviation, which is the effect of an unconformity of unknown duration adding 25% variability to the true excursion amplitude.*

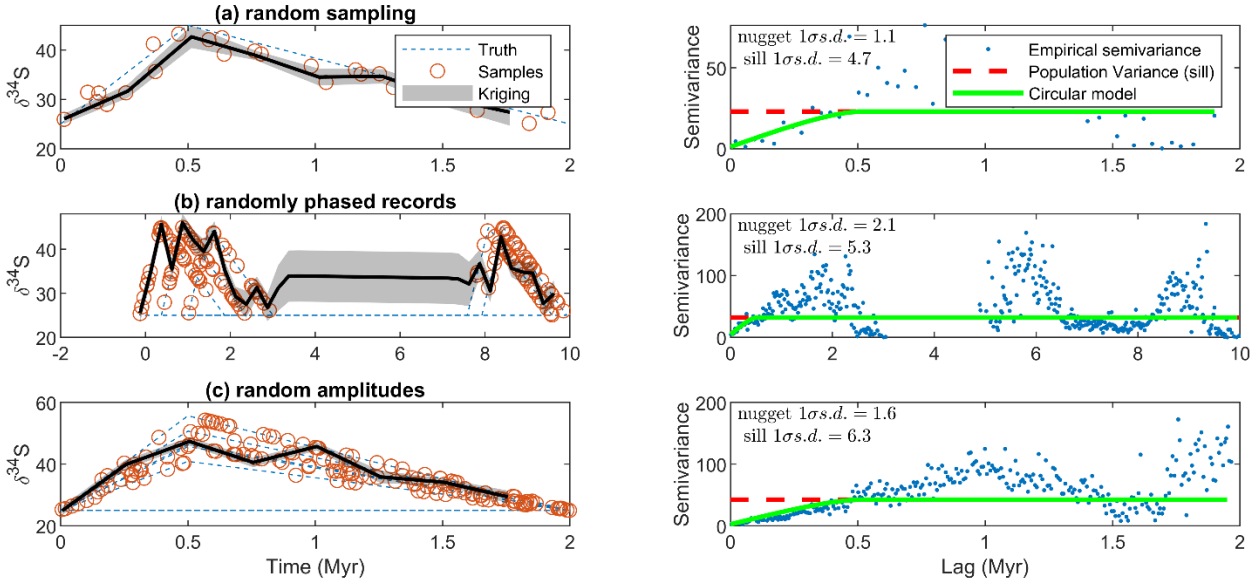

Supporting Figure S4. *Estimation of unresolved variance due to staggering multiple synthetic $\delta^{34}S$ excursions that have a duration of 2 Myr and amplitude of 20‰ (*cf. *Supporting Figure S3b). The nugget estimate is determined as the average nugget of 25 bootstrap samples of 1 to 5 synthetic excursions randomly misaligned with a standard deviation up to 5 times the length of the excursion (i.e., 10 Myr). A maximum nugget effect due to record misalignment occurs if the records are all randomly misaligned by about half of the excursion's duration.*

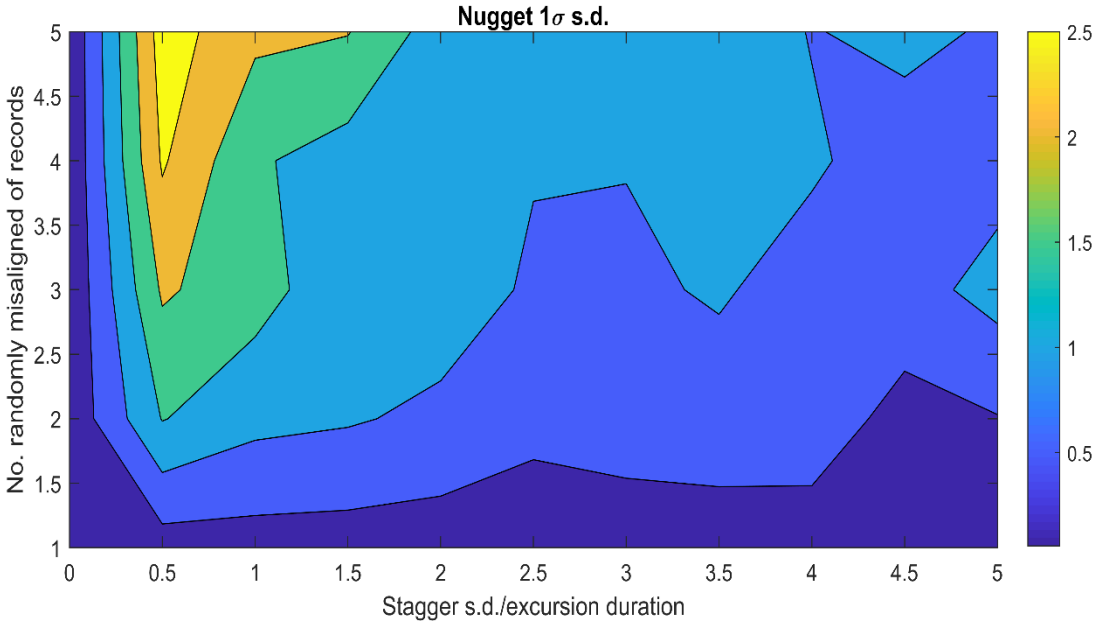

Supporting File d34S_Data.xlsx. *This Microsoft Excel spreadsheet contains all compiled $\delta^{34}S$ values, their assigned age, the proxy material from which they derive, and their source reference.*

Supporting Table S1. *Statistical description of all Phanerozoic $\delta^{34}S$ data. SD = standard deviation. CI = confidence interval.*

	n	mean	SD	median (95% CI)	skewness
Evaporite	1581	19.41	7.98	17.10 (16.76 – 17.44)	1.82
Biogenic CAS	912	18.87	5.14	18.80 (18.41 – 19.19)	0.28
Bulk CAS	3795	24.18	9.62	23.70 (23.38 – 24.02)	-0.48
Barite	422	19.50	2.22	19.15 (18.83 – 19.47)	-0.10
All data	*6710*	*22.04*	*8.79*	*21.08(20.86 – 21.30)*	*0.23*

Supporting Table S2. *References for $\delta^{34}S$ data included in compilation; number of CAS, evaporite, and barite analyses in each reference; and description of age assignments for the data.*

Reference	CAS	Evap.	Bar.	Age Model and Notes
Adams et al. (2010)	16			Ages linearly interpolated between Ar/Ar dates in provided in Figure 1 in paper. Stratigraphic heights extracted graphically.
Arp et al. (2008)	6			Assigned age of 146 Ma for the latest Tithonian
Ault & Kulp (1959)		12		Evaporite ages updated to latest stratigraphy. Omitted salt dome (migrated) samples from Feely & Kulp (1957), and only included samples with formation tabulated
Balderer et al. (1991)		11		Data compiled with age model by Bernasconi et al. (2017). Omitted vein and sandstone cement anhydrite samples.
Baldermann et al. (2015)	8			Linear interpoloation of stratigraphic height between Rb/Sr ages in paper
Bernasconi et al. (2017)		282		Age model provided in paper
Boschetti et al. (2011)		8		Data compiled with age model by Bernasconi et al. (2017)
Burdett et al. (1989)	56	25		Linear interpolation of stage boundaries from Berggren et al. (1985) to ICS2016/04 timescale. Ages and $\delta^{34}S$ extracted graphically from Figure 3.
Buschendorf et al. (1963)		24		Evaporites updated to latest stratigraphy. Omitted sulfide and barite samples.
Chen et al. (1981)		52		Translated from Chinese by Sang Chen, and $\delta^{34}S$ extracted graphically from figures. Only included Cambrian-Ordovician evaporites for which locality and unit could be determined.
Chen et al. (2013)	71			Linear interpolation of stratigraphic height between conodont zone age constraints from Kaufmann (2006), updated to GSSP ages in ICS2016/04
Claypool et al. (1980)		272		Evaporite ages updated to latest stratigraphy
Cortecci et al. (1981)		30		Used age model in Bernasconi et al. (2017), and assigned additional data from Western Alps to Rhaetian (Loprieno et al., 2011)
Dahl et al. (2019)	35			Ages provided in paper
Das et al. (1990)		6		Updated Michigan Basin chronostratigraphy from Rine et al. (2017)
Davies & Krouse (1975)		23		Evaporite ages updated to latest stratigraphy
Edwards et al. (2018)	117			Age model provided in paper
Fanlo & Ayora (1998)		26		Data compiled with age model by Bernasconi et al. (2017)
Fike & Grotzinger (2008)	157			Ages provided in Fike et al. (2015)
Fox & Videtich (1997)	13			Evaporite ages updated to latest Williston Basin stratigraphy using Taki & Pratt (2012)
Gill, Lyons, & Jenkyns (2011)	105			Linear interpolation of stratigraphic height between stage boundaries using ICS2016/04, assigning Calcari Maculati to Bajocian stage

Reference	CAS	Evap.	Bar.	Age Model and Notes
Gill, Lyons, Young, et al. (2011)	111			Linear interpolation of stratigraphic height between stage boundaries
Gill et al. (2007)	74			Linear interpolation of stratigraphic height between stage boundaries
Gomes et al. (2016)	115			Ages provided in paper on GTS2012 time scale, which matches ICS2016/04 in the Cretaceous
He et al. (2019)	165			Ages provided in paper for Siberian CAS data. For South China, age linearly interpolated by stratigraphic height between ICS2016/04 age of 529 Ma assigned to FAD of *W. crosby*i at base of Dahai Mbr, and age of 526.5 Ma to base of Shiyantou Fm. (Yang et al., 2018)
Hitchen & Krouse (1972)		6		Evaporite ages updated at stage scale to latest stratigraphy; omitted non-marine recent and migrated salt dome samples
Holser & Kaplan, Chem. Geol. (1966)		49		Evaporite ages updated to latest stratigraphy. Omitted salt dome (migrated) and secondary (cements/vugg-filling/intrusive igneous) textures
Horacek et al. (2010)		6		Data compiled with age model by Bernasconi et al. (2017)
Hovorka et al. (1993)		34		Assigned Delaware Basin ages from Wu et al. (2020) and Kerans and Tinker (1999). Data extracted graphically from Figure 5.
Hurtgen et al. (2009)	30			At Felix Cove, carbon isotope maxima in SPICE is set as base of Steptoean (Saltzman et al., 2004). In other sections, biomere event at onset of SPICE is set as base of Steptoean. March Pt. Formation includes *Bolaspidella* trilobites (Upper Middle Cambrian), and total deposition likely 5-10Ma; the lowest sample in the March Pt. Formation is set as the base of the Marjuman. Straigraphic heights extracted graphically.
Insalaco et al. (2006)		23		Age model provided by Bernasconi et al. (2017)
John et al. (2010)	34			Linear interpolation of stratigraphic height between conodont zone age constraints from Kaufmann (2006), updated to GSSP ages in ICS2016/04. Stratigraphic heights extracted from Fig. 4 and 5 graphically
Johnson et al. (2020)	130			Ages provided in paper interpolated to ICS2016/04
Jones & Fike (2013)	42			Linearly interpolated between stage boundaries using ICS2016/04. Hirnantian and Ordovician-Silurian boundary placed based on carbon isotope stratigraphy, not biostratigraphy, in text.
Kah et al. (2016)	42			Ages provided in Fig 9, using ICS2016/04 ages at the tie points
Kaiho et al. (2006)	11			Approximated age model as described for Schobben et al. (2017)
Kaiho et al. (2001)	12			Meishan section bed ages and accumulation rates from Burgess et al. (2014). Data tabulated in Kaiho et al. (2006)
Kaiho et al. (1999)	18			K-Pg boundary set at ICS2016/04 age, and sedimentation rates from paper. Data extracted graphically from Figure 3

Reference	CAS	Evap.	Bar.	Age Model and Notes
Kampschulte & Strauss (2004)	244			Ages updated by interpolation to ICS2016/04 from Harland 1989 Timescale (Harland et al., 1990). Data tabulated in Kampschulte (2001) and Kampschulte et al. (2001)
Kramm & Wedopohl (1991)		9		Zechstein evaporites tied to ICS2016/04 using ~1Myr/unit starting at the bottom of the Lopingian (Stollhofen et al., 2008)
Korte et al. (2004)	5			18.5m correlated by Gorjan & Kaiho (2007) to 250.7 Ma age in Bowring et al. (1998); linearly interpolated with *H. Parvus* FAD from Burgess et al. (2014)
Kozik et al. (2019)	48			Ages provided in paper in Fig. 3 based on Sr isotope stratigraphy by Saltzman et al. (2004)
Li et al. (2009)	27			Bed 27/28 boundary is proposed Permian-Triassic Boundary; using age from Burgess et al. (2014). Maokou/Wujiaping Fm. boundary is Guadalupian-Lopingian Boundary according to Yadong et al. (2008); using age from ICS2016/04. Data extracted from figures graphically.
Longinelli & Flora (2007)		8		Data compiled with age model by Bernasconi et al. (2017)
Loyd et al. (2012)	63			Linear interpolation of stratigraphic height between stage boundaries using ICS2016/04
Lu & Meyers (2003)		16		Middle Messinian age assigned in ICS2016/04
Luo et al. (2010)	58			Base of microbialite in Cili section correlated to base of Bed 25 in Meishan, and assigned age from Burgess et al. (2014); linearly interpolated height with FAD of *H. Parvus* assigned age from Burgess et al. (2014)
Lyu et al. (2019)	126			Ages provided in Fig. 8
Maharjan et al. (2018)	59			Linear interpolation of GTS2012 age model for conodont biostratigraphy provided in Fig. 1
Marenco et al. (2008)	25	9		Section correlated using flooding surfaces and Sr isotope data, and linearly interpolating ages of the Spathian/Anisian and Smithian/Spathian boundaries from Burgess et al. (2014)
Marenco et al. (2013)	20			Linear interpolation of stratigraphic height using stratigraphy published in Marenco et al. (2016), which uses ages in ICS2016/04. Data table appears truncated in publication; stratigraphic height and $\delta^{34}S$ extracted graphically from Fig. 4
Marenco et al. (2016)	7			Linear interpolation of stratigraphic height between stage boundaries in Fig 2, using ages from Kah et al. (2016), which match ICS2016/04
Meng, Zhang, Yan, et al. (2019)		5		Kept middle/upper Darriwilian assignment consistent with biostratigraphy and carbon isotope stratigraphy
Meng, Zhang, Schiffbauer, et al. (2019)		12		Tarim basin trilobite stratigraphy from Zhu et al. (2019). Includes one Lower Ordovician data from Cai et al. (2001) constrained to Tremadocian (Guo et al., 2018).
Mills et al. (2017)	114			Age model developed in paper on GTS2012 time scale, which matches ICSv2016/04 in the Cretaceous

Reference	CAS	Evap.	Bar.	Age Model and Notes
Newton et al. (2004)	32			Linear interpolation of stratigraphic height over the extinction interval using ages from Burgess et al. (2014), and age of 251.5 Ma for top of Tesero Ooilite set as the age at which the $\delta^{13}C$ returns to a "flat" value at the Meishan GSSP
Newton et al. (2011)	85			Linear interpolation of stratigraphic height between stage boundaries using ICS2016/04 for Yorkshire section, and correlated Tibet strata using chemostratigraphy preferred by the authors
Nielsen & Ricke (1964)		51		Evaporite ages updated to latest stratigraphy. Omitted caprock, stratigraphically unconstrained samples, lacustrine and freshwater-influenced samples, and Mg and K sulfates
Ohkouchi et al. (1999)	27			Age model based on Al accumulation provided in paper, and shifted +0.29 Myr to agree with ICS2016/04 Cenomanian-Turonian boundary age of 93.9Ma. Ages and $\delta^{34}S$ extracted graphically from Fig. 3A.
Owens et al. (2013)	216			Eastbourne section sedimentation rates between carbon isotope excursion features from Voigt et al. (2008) astrochronology tied to ICS2016/04 time scale using Cenomanian-Turonian GSSP. South Ferriby and Trunch sections tied to ages of CIE calculated for Eastbourne section and linearly interpolated stratigraphic height. Raia del Pedale section height linearly interpolated between CIE ages from Eastbourne and stage boundaries.
Pankina et al. (1975)		18		Evaporite ages updated to latest stratigraphy
Paytan et al. (1998)			69	Ages updated to ICS2016/04 from those provided in Kurtz et al. (2003), which uses Berggren et al. (1995) timescale. Ages for Sites 305, 366, and 577 updated to ICS2016/04 from those provided in Yao et al. (2020).
Paytan et al. (2004)			123	Ages updated to GTS2004 by Prokoph et al. (2008), and then interpolated to ICS2016/04
Peryt et al. (2010)		52		Evaporite ages updated to latest stratigraphy
Pisarchik & Golubchina (1975)		17		Evaporite ages updated to latest stratigraphy; omitted Vendian Motyi Formation
Playà et al. (2007)		10		Age of 70 kyr given in text
Posey & Fisher (1989)		59		Assigned Kungarian to lowermost Roadian age to reconcile top-Wolfcamp correlations between Midland and Palo Duro basins (Blomquist, 2016; Handford & Dutton, 1980; Mazzullo, 1982). Interpolated correlated wells as in Fig. 3
Poulton et al. (2015)	24			Sedimentation rates from Kolonic et al. (2005), rescaled to reflect obliquity-controlled cycles instead of eccentricity, as the authors prefer, citing Meyers et al. (2012). Cenomanian-Turonian boundary shifted from GTS2004 age in Kolonic et al. (2005) to ICS2016/04.
Present et al. (2015)	77			Ages determined by linearly interpolating stage boundaries, which are placed with carbon isotope stratigraphy as described by Jones & Fike (2013)

Reference	CAS	Evap.	Bar.	Age Model and Notes
Present (2018, Ch. 3)	52			ICS2016/04 ages used to interpolate biostratigraphy and carbon isotope stratigraphy in Bergström et al (2009) and Cramer et al. (2010)
Present et al. (2019)	255			Linearly interpolated stratigraphic height between high frequency sequence boundary ages in Wu et al. (2020)
Rennie & Turchyn (2014)	56			Site 807A to 362.8m: Martin & Scher (2004); Site 807A below 362.8m: Schrag et al. (1995); Site 821A: Wei & Gartner (1993); Site 1003A: Wright & Kroon (2000)
Rennie et al. (2018)	119			Age model provided in paper
Riccardi et al. (2006)	102			Used Burgess et al. (2014) ages for Meishan section and extinction interval at Shangsi, and for Dienerian base. Used Algeo et al. (2013) age for Changhsingian base. Used Bowring et al. (1998) age for base of Meishan bed #7.
Richardson et al. (2019)	93			Linearly interpolated ages with stratigraphic height given in Fig. 4
Rose et al. (2019)	118			Linearly interpolated stratigraphic height between Datum 2 bentonite age of 431.8 Ma and top of Sheinwoodian Sub-stage 2 from Cramer et al. (2012)
Sakai (1972)		13		Evaporite ages updated to latest stratigraphy. Omitted Precambrian samples, and samples purposely chosen to have anomalously-low $\delta^{34}S$
Schobben et al. (2015)	74			Ages provided in paper using Burgess et al. (2014) dates
Schobben et al. (2017)	19			Assigned approximate mid-Griesbachian age of 251.50 Ma to uppermost Balvany East strata, and linearly interpolated stratigraphic height to Permian-Triassic Boundary at base of Gerennavar Fm., neglecting missing section between Balvany East and Balvany North; used same accumulation rate for limestones in Nagyvisnyo Fm. anchored at EPME and apportioned remaining time in the Boundary Shale beds between top of limestones and P-Tr. Boundary
Schroder et al. (2004)		29		Ages provided in Fike et al. (2015)
Sim et al. (2015)	68			Ages provided in paper using Kaufmann (2006) time scale updated to GSSP ages in ICS2016/04
Solomon et al. (1971)		27		Evaporite ages updated at stage scale to latest stratigraphy
Song et al. (2014)	202			Age model is from Figure 4 (tie points are in bold), using dates from Burgess et al. (2014) and ICS2016/04; interpolated linearly in between tie points; Composite height is linking of sections by the C-isotope tie points in Figures 3 and 4: Daijang 400m = Lower Guandau 135m (N3); Lower Guandau 225m = Upper Guandau 10m (P4). Adjusted Daijang B by 18m to approx. bring in line with Daijang A, as in Fig 3

Reference	CAS	Evap.	Bar.	Age Model and Notes
Song et al. (2019)	29			Age model tied to Song et al. (2014) using correlation in Fig. 8 by linearly apportioning height between 40m and 48m to gap at Smithian-Spathian Boundary between 139.2m and 163m at Lower Guandau, and Burgess et al. (2014) age for base of Smithian at base of section
Spötl (1988)		8		German-language data compiled and assigned ages by Bernasconi et al. (2017)
Stebbins et al. (2019)	75			Age model provided in Supplemental Figure S4
Thode & Monster (1965)		68		Evaporite ages updated to latest stratigraphy. Data is reported as the range of measurements, so only could include the maximum and minimum values in compilation; omitted poorly-constrained intervals.
Thode & Monster (1970)		17		Evaporite ages updated at stage scale to latest stratigraphy
Thode et al. (1958)		5		Assigned to upper Frasnian (Hearn et al., 2011)
Thompson & Kah (2012)	235			Ages provided in paper using U/Pb dates in Thompson et al. (2012). Data tabulated in Thompson (2011).
Turchyn et al. (2009)	39		39	Ages updated by interpolation to ICS2016/04 from GTS2004
Utrilla et al. (1992)		62		Listed formations assigned by stage to ICS2016/04 ages. Omitted continental evaporite formations.
van Everdingen et al. (1982)		70		Evaporite ages updated to latest stratigraphy. Omitted vein gypsum.
Vinogradov (2007)		23		Toyonian evaporites assigned in 1 Myr intervals by subformation (Novikov, 2017)
Vredenburgh & Cheney (1971)		16		Evaporite ages updated to latest stratigraphy. Omitted "sulfur crusts."
Witts et al. (2018)	41			Linearly interpolated magnetochronological age assignments using stratigraphic heights.
Worden et al. (1997)		11		Used age model in Bernasconi et al. (2017)
Wotte et al. (2012)	85			Linear interpolation of stratigraphic height between stage boundaries
Wotte et al. (2011)	69			Linear interpolation of stratigraphic height between stage boundaries, using Susan Duster Limestone sedimentation rate for Molodo River and Ulakhan-Kyyry-Taas sections
Wu et al. (2014)	214		66	Ages updated by interpolation to ICS2016/04 from GTS2004. Data tabulated in Wu (2013).
Yan et al. (2013)	27			Guadalupian-Lopingian boundary set at base of *C.p.p.* based on ICS2016/04; Sedimentation rate from Qiu et al. (2015) indicate 0.04cm/kyr in the bedded chert relative to bentonite (257 Ma) at top of *C.p.p* zone, so base of bedded chert is 258.6 Ma.; applied this sed rate down through the limestone
Yao et al. (2018)			58	Age model provided in paper relative to PETM, which is taken as 55.93 Ma after Westerhold et al. (2008)
Yao et al. (2020)			88	Ages updated by interpolation to ICS2016/04 from GTS2012

Reference	CAS	Evap.	Bar.	Age Model and Notes
Yeremenko & Pankina (1972)		17		Evaporite ages updated to latest stratigraphy
Young et al. (2016)	68			Linear interpolation of stratigraphic height between stage boundaries in Fig 2 and 3
Young et al. (2019)	40			Assigned base and top of Ireviken CIE to bentonite age of 431.8 Ma and top of Sheinwoodian Sub-stage 2 (430.2 Ma) from Cramer et al. (2012) for Roberts Mtn. section. Aligned Newsom Roadcut carbon isotope record with Roberts Mtn. section, with unconformity on rising limb
Zhang et al. (2015)	15			Used Smithian/Spathian boundary ages from Burgess et al. (2014) and sedimentation rates provided in Figure 3

199